PAPER • **OPEN ACCESS**

Effects of humidity on the dynamics and electron recombination of a pin-to-pin discharge in He + H_2O at atmospheric pressure

To cite this article: Alexandra Brisset *et al* 2022 *Plasma Sources Sci. Technol.* **31** 045008

View the article online for updates and enhancements.

You may also like

- Bell nonlocality in networks
Armin Tavakoli, Alejandro Pozas-Kerstjens, Ming-Xing Luo et al.
- Modeling inductive radio frequency coupling in powerful negative hydrogen ion sources: validating a self-consistent fluid model
D Zielke, S Briefi, S Lishev et al.
- Simple Analytic Formula Relating the Mass and Spin of Accreting Compact Objects to Their Rapid X-Ray Variability
Gabriel Török, Andrea Kotrlová, Monika Matuszková et al.

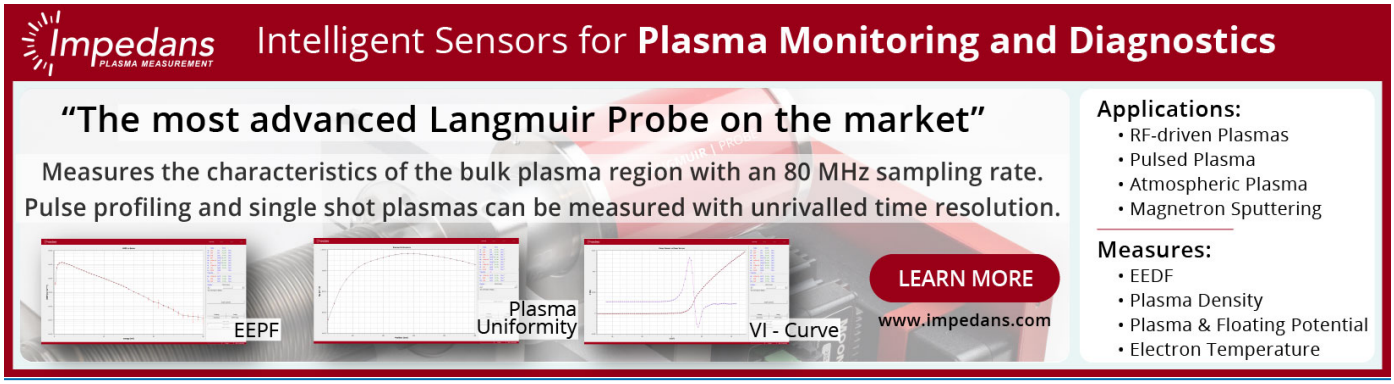

This content was downloaded from IP address 86.134.222.212 on 24/04/2022 at 08:39

OPEN ACCESS
IOP Publishing
Plasma Sources Science and Technology
Plasma Sources Sci. Technol. **31** (2022) 045008 (12pp)
https://doi.org/10.1088/1361-6595/ac6130

Effects of humidity on the dynamics and electron recombination of a pin-to-pin discharge in He + H_2O at atmospheric pressure

Alexandra Brisset[1], Benjamin Harris[1], Aaron Dickenson[2], Kari Niemi[1], James Walsh[2] and Erik Wagenaars[1]

[1] York Plasma Institute, Department of Physics, University of York, York YO10 5DD, United Kingdom
[2] Department of Electrical Engineering and Electronics, University of Liverpool, Liverpool, Merseyside, United Kingdom

E-mail: erik.wagenaars@york.ac.uk

Received 20 September 2021, revised 23 February 2022
Accepted for publication 25 March 2022
Published 14 April 2022

Abstract

Control of the plasma chemistry is essential for the effectiveness of atmospheric pressure plasmas in many applications. For this, the effects of the humidity of the feed gas on the discharge chemistry need to be considered. Detailed studies are scarce and many of them are dominated by surface interactions, obscuring any volume effects. Here, a negative nanosecond pulsed discharge is generated in a pin–pin 3 mm gap geometry in He + H_2O that enables the study of volume kinetics due to minimal surface area. The effect of humidity on the discharge development, electric field and electron density is investigated through experiments and modelling. It is found that the presence of water vapour affects both the electron density at the start of the pulse (remaining from the previous pulse) and the ionisation rates during the ignition phase, leading to a complex dependence of the discharge development speed depending on the water concentration. The electron decay is studied using the 0D global kinetics model GlobalKin. The dominant reactions responsible for the electron decay depending on the concentration of water vapour are determined by comparing experimental and simulated results and these reactions are grouped in simplified kinetic models. It is found that with water concentrations increasing from 0 to 2500 ppm, the complexity of the dominant reactions increases with in particular O_2^+, $H_2O_3^+$ and water clusters becoming important for high water concentrations. This work also provides experimental data for validation of kinetic models of plasmas in controlled environments.

Keywords: nanosecond discharge, Stark broadening, electron recombination, electric field

(Some figures may appear in colour only in the online journal)

* Author to whom any correspondence should be addressed.

Original content from this work may be used under the terms of the Creative Commons Attribution 4.0 licence. Any further distribution of this work must maintain attribution to the author(s) and the title of the work, journal citation and DOI.

 © 2022 The Author(s). Published by IOP Publishing Ltd

1. Introduction

Atmospheric pressure discharges can achieve the needs of many applications through the control of the plasma chemistry [1–11]. This control can be approached by source design, feed gas control or voltage waveform choices. In particular, the use of nanosecond pulsed discharges with high voltage rise rates (>1 kV ns^{-1}) has gained major interest in recent years because these discharges combine a great stability and a good energy efficiency in terms of radical species production at low gas temperature [12–15]. They are used for the production of nanomaterials, catalysis, CO_2 conversion and plasma medicine. One element of interest of high voltage rise rates is to induce the ignition of the discharge at a higher electric field than that required for breakdown. In this work, the voltage remains relatively moderate with a rise rate of 1.5 kV ns^{-1}, nevertheless ensuring high stability and reproducibility of the discharge.

Several models were developed to capture the physics and chemistry of He plasmas with small amounts of water vapour and air to tailor the gas chemistry [8, 16, 17]. The breakdown voltage and ionic composition, both being strongly affected by impurities, are studied in detail, as well as the species fluxes relevant for biomedical applications. For instance, in a He + air + water DBD [17], it was shown numerically that introducing low amounts of water (<few hundred ppm) decreases the breakdown voltage, resulting in lower electric fields and a slower development of the discharge. For higher amounts of water, attachment processes resulted in an increase of the breakdown voltage. However, most of these studies are relevant for parallel-plane electrode configurations characterised by relatively low electric fields and large losses of charged particles to the walls. In reference [8], electron losses are entirely due to losses at the walls with water concentrations below 10 ppm and only 12% of electron losses are due to other processes at 1000 ppm H_2O (electron attachment and electron–ion recombination). This limits the possibility to study gas-phase chemistry with these discharges, in particular for the afterglow phase. In a pin–pin configuration, processes at the walls are much weaker, allowing for the study of gas phase processes, in particular those governing the electron decay.

In literature, electron recombination processes have been studied in dry helium by Thomson scattering and optical emission spectroscopy (Stark broadening). Roettgen *et al* [18] measured electron densities in the range 3.5×10^{21} m^{-3} in a high current (60 A), high power (12 mJ) filamentary discharge at moderate pressure (100–200 Torr). At such high ionisation rates, the electron distribution is nearly Maxwellian and the discharge can be described quite well with classic fluid models. It is asserted that the electron decay is due to dissociative recombination of He_2^+ ions, forming metastable and ground state helium. At atmospheric pressure, Carbone *et al* [19, 20], reintroduced a fast three body recombination process that would produce high energy Rydberg states instead of the more commonly assumed metastable states. The general importance of this reaction in other discharges is still a subject of debate. Other works studied the effect of water vapour on the electron recombination of pin–ring air [21] and high repetition frequency argon [22] discharges, that both showed a strong decrease of the electron recombination time due to recombination with water clusters or H_3O^+, respectively. In this work, we attempted to build simplified kinetic models to describe the electron recombination in the afterglow both in dry and humid helium.

In this paper, grounds for chemistry tailoring studies are set with the comparison of experimental and numerical characterisation in a reference condition of a pin-to-pin ns-pulsed glow discharge in He with controlled amounts of water vapour. The source design was chosen to study volume kinetic processes with limited contact with the electrodes. Electric field, electron density and gas temperature are measured by optical emission spectroscopy and analysed using a 0D plasma-chemical kinetics model. The effect of humidity on the discharge propagation is studied and dominant reaction pathways of electron decay as a function of water vapour concentration are identified, leading to proposed simplified reaction sets for different concentrations of water vapour.

2. Experimental setup

2.1. Discharge setup

The general setup is described in figure 1(a). The discharge is generated in helium (99.996% purity) by using a pin-to-pin electrode geometry. The electrodes are placed in a 0.3 l vessel and are 3 mm apart. They are symmetric, both made of stainless steel and have a radius of curvature of approximately 500 μm. A negative high-voltage nanosecond pulse is applied to one of the pins by means of a high voltage DC supply coupled to a home-made switch box delivering a negative 2.7 kV voltage pulse of ∼2 ns rise time and about 100 ns duration [see figure 1(b)]. The discharge is run at 5 kHz. The voltage is measured using a high bandwidth probe (Tektronix P5100A 500 MHz). The current is measured by an ion physics probe—CM-100-M, 1.0 V A^{-1}. The applied voltage and the discharge current are recorded with a 1 GHz–10 Gs s^{-1} digital oscilloscope (LeCroy wavesurfer10). A total controlled flow rate of 3 l min^{-1} is injected sideways to the electrodes' axis. Water vapour is admixed to the gas flow using two mass flow controllers. A defined content of water vapour is added to the feed gas by guiding a fraction of the total helium flow through a glass bubbler filled with distilled water as in [6]. The amount of water vapour is calculated using the vapour pressure at room temperature and the flow rate through the bubbler. Most of the lines are made of stainless steel to limit the impurities in the gas. The output gas of the reactor is guided to an exhaust several metres downstream.

2.2. Optical diagnostics and procedures

2.2.1. Detection system for discharge imaging and optical emission. The UV–visible wavelength-integrated emission of the discharge is recorded with a 4Picos ICCD camera from Stanford Computer Optics with a temporal resolution of 6 ns.

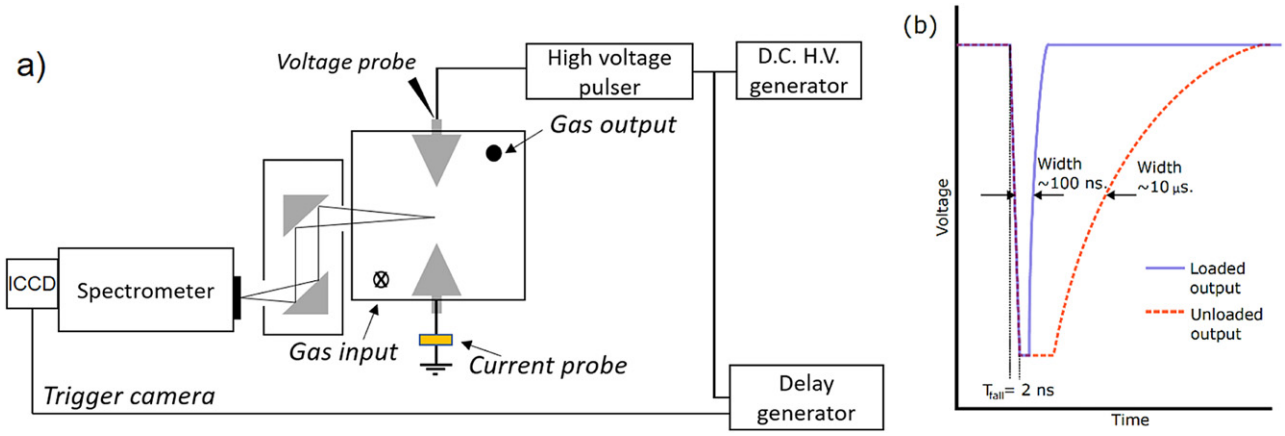

Figure 1. (a) Scheme of the discharge and absorption spectroscopy setup. (b) Diagram showing impact on output pulse shape with loaded and unloaded output, due to the design of the in-house pulse generator developed (employed transistors are operating in the avalanche mode, in a Marx bank configuration, to achieve rapid switching times).

The temporal resolution considers the 5 ns jitter of the discharge and the 1 ns camera gate width. Thanks to the very good spatial stability of the discharge, an average over 50 discharges is made for each recorded image. These fast imaging measurements are used to estimate the propagation speed of the discharge.

Optical emission spectroscopy is done by focussing the plasma emission into an 0.5 m Czerny–Turner spectrograph (Andor SR500i) equipped with an iStar Andor ICCD camera (DH334T-18U-C3). Two parabolic mirrors [UV enhanced aluminium parabolic mirrors (Thorlabs, MPD-F01)] are used to focus the plasma emission to the spectrometer slit, limiting chromatic aberrations. To determine the gas temperature from the analysis of the rotational structure of the transition $N_2(C–B)(v' = 0, v'' = 0)$, a 2400 l mm^{-1} grating is used with a slit aperture of 40 μm, giving a spectral resolution of 0.03 nm. The line broadening of hydrogen lines is studied using the same settings. For those two experiments, the plasma emission is recorded along the axis of the discharge and is line of sight integrated in the direction perpendicular to the discharge. The time resolution is 9 ns including 4 ns camera gate width.

2.2.2. Procedure for electron density measurement. The electron density is estimated by analysing the line broadening of hydrogen emission lines H_β (486.135 nm). Several phenomena induce the broadening of emission lines and the formula used to describe the line broadening of each of these phenomena was taken from the following references [23–27]. It should be noted that in these references, the formula sometimes correspond to different quantities, in particular the broadenings given in reference [25] correspond to the half width half maximum of the line while they correspond to the full width half maximum (FWHM) in references [23, 24]. Here, the FWHM is used.

The Doppler contribution to the line broadening is of the form: $\Delta\lambda_D(\text{FWHM}) = 3.48 \times 10^{-4}\sqrt{T_g}$. It will be shown in section 4.2 that the gas temperature stays close to 340 K $\pm$ 10 K during the discharge for any gas mixture giving $\Delta\lambda_D =$ 0.0064 nm.

The Van der Waals contribution is $\Delta\lambda_{VdW}(\text{FWHM}) = \frac{2.4}{T_g^{0.7}}$, the factor 2.4 is taken from [24] according to the method of [25]. For gas temperatures of 340 K $\pm$ 10 K, this gives Van der Waals broadening in the order of 0.0406 nm $\pm$ 8 $\times$ 10^{-4} nm, which is not insignificant compared to the Stark broadening and therefore needs to be considered in the analysis.

The resonant contribution is $\Delta\lambda_{res}(\text{FWHM}) = 30.2{*}X_H\frac{P(\text{atm})}{T_g(\text{K})}$ where X_H is the molar fraction of H, taken from [25]. In this study, even for the highest possible values of X_H (complete dissociation of water for the highest humidity level, $X_H = 0.005$), the contribution for the resonant contribution is negligible (4 $\times$ 10^{-4} nm).

The instrumental profile was measured with a Hg/Ar Pen-Ray lamp using two Hg lines at 435.7 nm and 491.5 nm to make sure that the instrumental function was not varying with the wavelength. The instrumental profile is not Gaussian, it has a non-negligible Lorentzian contribution. To extract the Stark broadening from the total line broadening, the following procedure is therefore applied: (1) the experimental instrumental profile is convolved with a Lorentzian function of arbitrary width (2) the resulting function is fitted to the experimental hydrogen line using the width as the fitting parameter (3) the Van der Waals contribution is subtracted from the width obtained for the best fit.

Finally, the electron density is determined from the Stark broadening using: $\Delta\lambda_{Stark} = 4.8(\text{nm}) * \left(\frac{n_e}{10^{23}(\text{m}^{-3})}\right)$ [27]. These measurements are done after the electric field has dropped below 1 kV cm^{-1}. In these conditions, the electric field does not affect the Stark broadening [28] and the presented formula is valid.

Figure 2 presents a typical experimental profile of H_β in humid He together with the fitting function made of the convolution of a Lorentzian function and the instrumental function (see section 2) and the same fitted function after subtraction of the Van der Waals contribution, showing the importance of including this contribution in the analysis.

2.2.3. Electric field determination. The electric field is obtained by analysis of the splitting of the H_β line. In the presence of an electric field, the energy levels of a hydrogen atom are split into $2n - 1$ sublevels that are polarised according to the principal (n) and magnetic (m) quantum numbers. The radiative emission is polarised and is usually decomposed into a polarisation π, linearly to the electric field E, and a polarisation σ, circular to E. With our spectral resolution, the emission lines are partially superimposed and an apparent splitting of the H_β line is observed as illustrated in figure 3. The electric field can be determined from the spectral distance of the two resulting peaks (Δ_{pp}) through [29]:

$$\pi \quad E(\mathrm{V\ cm^{-1}}) = \Delta_{pp}(\mathrm{nm}) \times (3.78 \times 10^4), \qquad (1)$$

$$\sigma \quad E(\mathrm{V\ cm^{-1}}) = \Delta_{pp}(\mathrm{nm}) \times (7.46 \times 10^4), \qquad (2)$$

In this work, the π polarisation of the H_β line at 486 nm is studied, by including a linear polariser in front of the spectrometer entrance.

3. Modelling

The 0D global plasma-chemical kinetics code GlobalKin, as described in detail in a previous paper [6], is used to study the kinetics of the present pulsed glow discharge. It consists of a reaction chemistry and transport module, a Boltzmann equation solver and an ordinary differential equation solver. In the ordinary differential equation solver, the mass continuity equations for each charged and neutral species are solved as a function of time accounting for surface and gas phase production and consumption processes. A few modifications were implemented compared to [6], in particular the two-term Boltzmann equation is solved over short 10^{-11} s time steps. Simulations are carried out for plasma electrodes of 0.1×0.1 cm^2 and a gap distance of 0.3 cm. The power density is determined experimentally from voltage and current waveforms. The reaction mechanism includes the same 46 species and 577 reactions as described in the appendix of [6] except for the reaction rate of the reaction labelled 99 in the reference [6] ($e + He_2^+ \rightarrow He + He(2^3S)$) due to its importance on the electron recombination rate. It was reviewed to 1.1×10^{-8} cm^3 s^{-1}, as reported in [30]. It should be noted that the $He(2^3S)$ state in the $He/H_2O/O_2$ reaction mechanism as it is written in [6] is not supposed to be state-specific. It is rather a lumped state of excited He and will therefore be written as He^* in this paper. Nevertheless, in effect, He^* species decay down to the $He(2^3S)$ in a few tens of ns [30].

It should also be noted that the model does not include a full treatment of VUV photons from He_2^* and V–T transfers as in [31, 32]. The loss of energy due to radiative emission, that is delivered mostly through electron impact and ionisation of He, is considered in the model but no process of re-distribution of that energy among excited states through radiation absorption in particular is considered. Even though, these effects are believed to be minor in our conditions, it cannot be fully excluded that these will have some impact on the ionization pathways of the discharge.

4. Results

4.1. Electrical and emission characteristics

The discharge is powered by a 2.7 kV negative nanosecond pulse of 2 ns rise time and about 100 ns width in a 3 mm gap. It is run at 5 kHz. The electrical signals, in dry He, are presented in figure 4. The current rise starts at 70 ns inducing the voltage drop. It can be seen that the current reaches 0 despite the maintenance of a low DC voltage after about 125 ns.

Such electrical signals are characteristic of a low density mode, as defined by Verreycken *et al* [24] for which the energy dissipation is of the order of a few tens of microjoules and the chemistry is concentrated in the centre of the plasma filament.

Fast imaging of spectrally integrated emission of the discharge, presented in figure 5, reveals a cathode-directed streamer followed by a slow backward wave. In dry helium, the discharge bridges the gap in about 30 ns and the discharge emission is most intense at around 80 ns. It corresponds to the instant of maximum amplitude of the current. At breakdown, hereafter defined as the instant the streamer reaches the grounded electrode, the voltage drops by about 500 V due to the increased gas conductivity induced by the streamer. After 100 ns, the discharge emission fades drastically.

Figure 6 presents the voltage and current signals in gas mixtures of various water vapour concentrations. In the presence of low amounts of water vapour, the current rise is delayed by a few nanoseconds compared to dry He. However, with increasing water concentration, the current rise happens earlier and precedes the current rise in dry helium. The current amplitude also increases with increasing water concentration from 1.2 A at 275 ppm H_2O to 1.6 A at 2500 ppm H_2O. The energy dissipated in the discharge stays the same within measurement uncertainty.

Fast imaging of the spectrally integrated emission of the discharge, similar to figure 5, provides further insight into the modification of the plasma development for varying concentrations of water in He. It was used to determine the propagation speed of the streamer and backward wave, by dividing the discharge gap (3 mm) by the time between images where the streamer and backward wave cross the gap (e.g. 0–30 and 30–52 ns respectively in figure 5). These propagation speeds for different amounts of water content are presented in figure 7. It clearly shows that the propagation speed of the streamer is slower in the presence of water vapour compared to dry helium, however it gets faster as the concentration of water vapour increases. On the contrary, the backward wave is always faster in the presence of any concentration of water vapour (see section 5 for a possible explanation). Consequently, whereas the discharge ignition and streamer propagation are faster in dry helium, the current rise happens earlier in the presence of moderate and high amounts of water vapour.

4.2. Gas temperature

The gas temperature is obtained by analysing the rotational distribution of the second positive system of nitrogen N_2(C–B, $v' = 0$–$v'' = 0$). For that specific experiment, 0.1% N_2 was

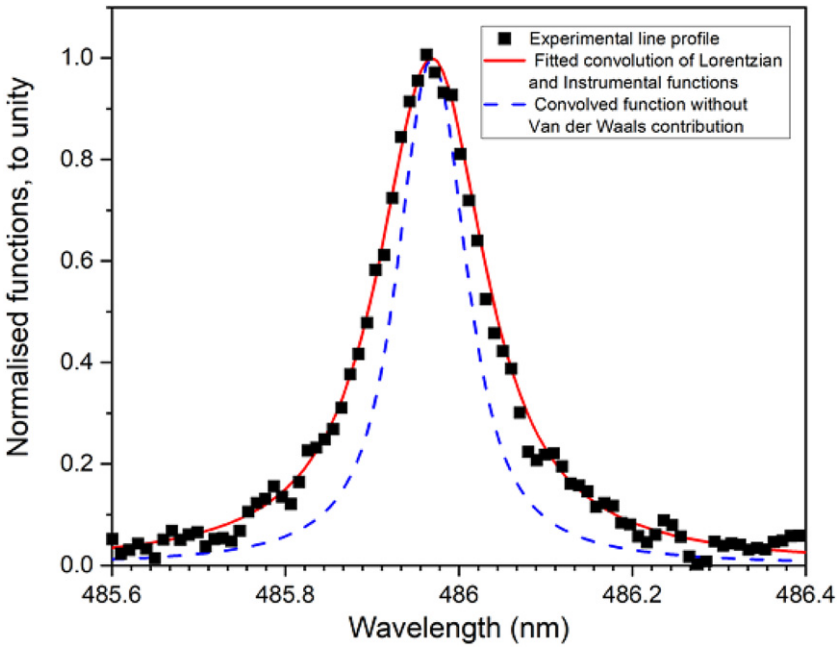

Figure 2. Typical experimental and fitted profile of H_β in humid He.

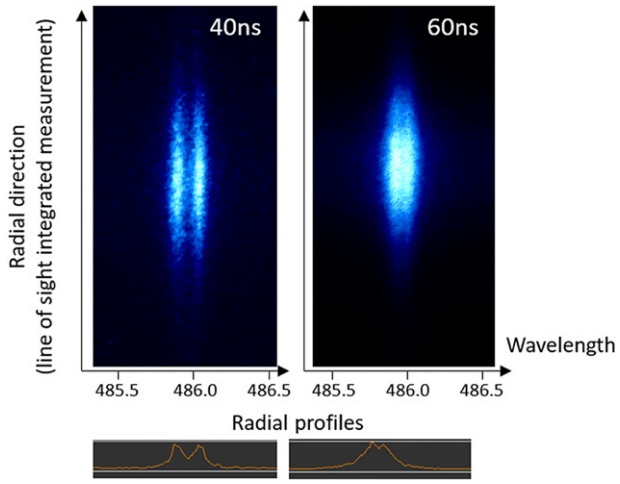

Figure 3. Illustration of the splitting of the H_β line in dry helium, at mid gap, along the radial axis, at 40 ns and 60 ns.

added to ensure a good signal without noticeably affecting the discharge characteristics. Among the commonly used excited states for gas temperature determination, $N_2(C)$ is the most reliable species for pulsed discharges in helium at atmospheric pressure [33, 34]. The experimental spectrum is fitted using the Massive OES software [35–37]. Figure 8 shows the best fit of a typical emission spectrum of $N_2(C–B)(0, 0)$ assuming rotational thermal equilibrium. No significant deviations to the experimental spectrum can be observed.

The gas temperature measured at the vicinity of the anode, ground electrode and in the centre of the gap with a spatial resolution of 1 mm are very similar and equal to 340 ± 15 K at any position in the gap and any time in the discharge. This value is used for derivation of the Van der Waals broadening of the hydrogen line and for kinetic reaction rates throughout the work. It is also consistent with the work of reference [38] for which the gas temperature was measured in a similar discharge by laser induced fluorescence (LIF) of OH and by analysis of the optical emission spectrum of the transition OH(A–X). It can be concluded that the discharge is sufficiently short to avoid any significant heating and any kind of thermal dissociation processes of species present.

4.3. Electric field and electron properties

Measurements of electric field and electron density at mid gap are presented in figure 9. The electric field could only be measured when the intensity of the emission of the hydrogen beta line was above noise level and above 1 kV cm^{-1} to discern the line splitting (see section 2.2). Therefore, the electric field could not be measured in the first nanoseconds, or tens of nanoseconds in dry helium, when the intensity of the hydrogen line is weak. Consequently, the passage of the streamer field front is captured in humid conditions but not in dry helium. On the other hand, the electron density could only be measured in the absence of line splitting, once the electric field has dropped below 1 kV cm^{-1}, which coincides with the rise of electron density. The instant of breakdown (streamer reaching the grounded electrode as determined by ICCD imaging) is represented by a vertical line in figure 9(b).

It appears that the electric field is moderate, below 10 kV cm^{-1} in the front but remains high in the channel of the negative streamer, for any gas mixture. The electric field in the channel remains about 7 kV cm^{-1} in dry helium and 5 kV cm^{-1} for >1000 ppm H_2O, before it drops at a rate of 0.1 kV cm^{-1} ns^{-1}. In this work, it should be noted that the time resolution of 9 ns as well as the spatial averaging, induce the averaging of the electric field between the front and the channel over the equivalent of about 1 mm length (considering the propagation speed of 8×10^4 m s^{-1}), meaning the

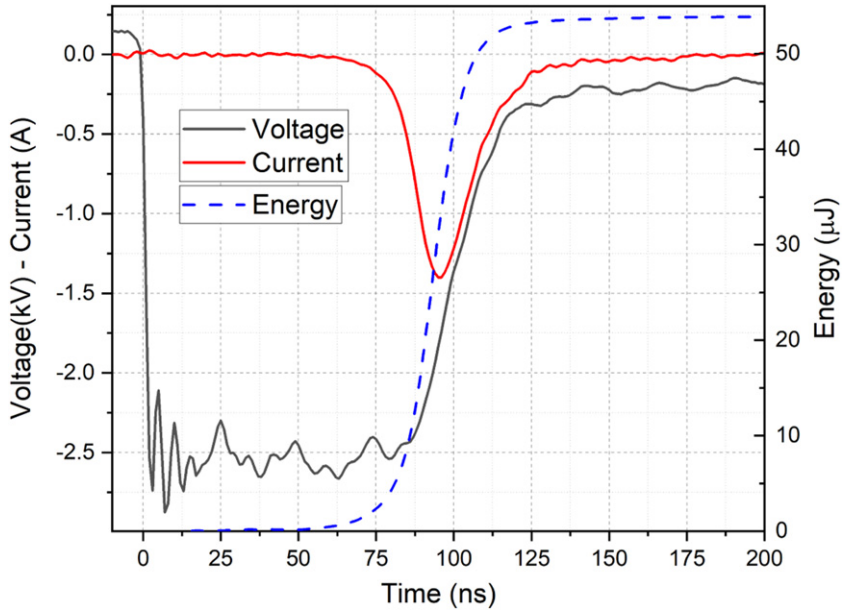

Figure 4. Voltage, current and energy signals up to 300 ns.

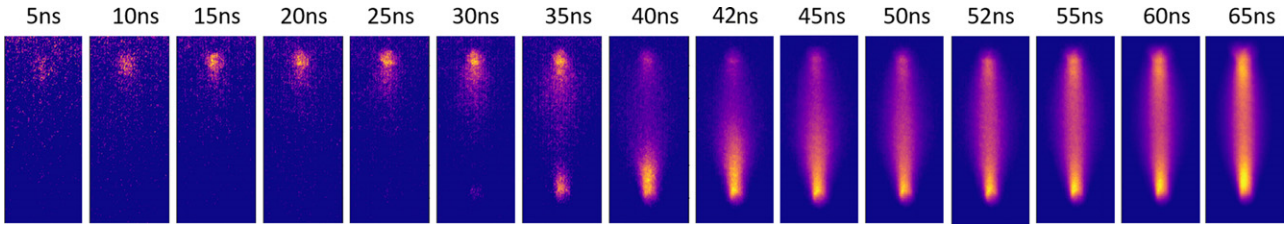

Figure 5. Fast imaging of the streamer propagation and of the backward wave in dry helium for a gap of 3 mm at −2.7 kV and 5 kHz. Voltage is applied to the top electrode, bottom electrode is grounded. The intensity scale is adapted for each image to show the light structure at each instant. Time resolution is about 6 ns. Propagation takes about 30 ns and backward wave takes about 22 ns.

electric field structure around a streamer head cannot be completely resolved. Nevertheless, the observed temporal profile is in line with expectation for a negative streamer. In [39], the electric field of the streamer of a helium plasma jet in air was estimated numerically and it was shown that the peak electric field is very moderate (about 11 kV cm^{-1}) and that in the channel, the electric field remained high, from about 2 to 6 kV cm^{-1} along the channel, contrary to positive streamers. This relatively smooth axial profile of the electric field from the front head to the channel of a negative streamer suggests that space and time-averaging effects are limited and the electric field front measured could be a good approximation, slightly underestimated, of the real electric field in the front.

In the presence of water vapour, the electric field decreases both in the discharge front and in the channel. This indicates a faster ionisation rate during the discharge development [40] and will be discussed in section 5.5.1.

After breakdown, the electron density starts to rise with the current during the backward wave. At mid gap, it reaches $2.7(\pm0.5) \times 10^{21}$ m^{-3} in dry helium and it decays with a rate of 1.2×10^{-14} m^3 s^{-1}. As the concentration of water vapour increases, the peak electron density decreases significantly. This could be due to a combination of lower electric fields, increased discharge radius at mid-gap and faster charge propagation.

5. Discussion

5.1. Discharge ignition and development in presence of water

It was reported in section 4 that the introduction of varying concentrations of water vapour induced complex effects in the helium discharge. First of all, it affects the discharge development as summarized in figure 7. The propagation speed of the discharge drops by a third with the addition of 275 ppm H_2O and the breakdown is delayed by 30 ns. However, as the concentration of water increases, the propagation speed increases progressively and for 2500 ppm H_2O case, it almost catches up with the speed in dry He. The speed of the backward wave shows a very different trend being significantly slower in dry He than in any humid condition. The drop of the propagation speed in humid helium could be due to the faster electron recombination with water in the discharge afterglow. Indeed, the fast decay in electron density measured in humid helium [figure 9(a)] suggests that the electron density at the start of a new pulse could be very low compared to dry

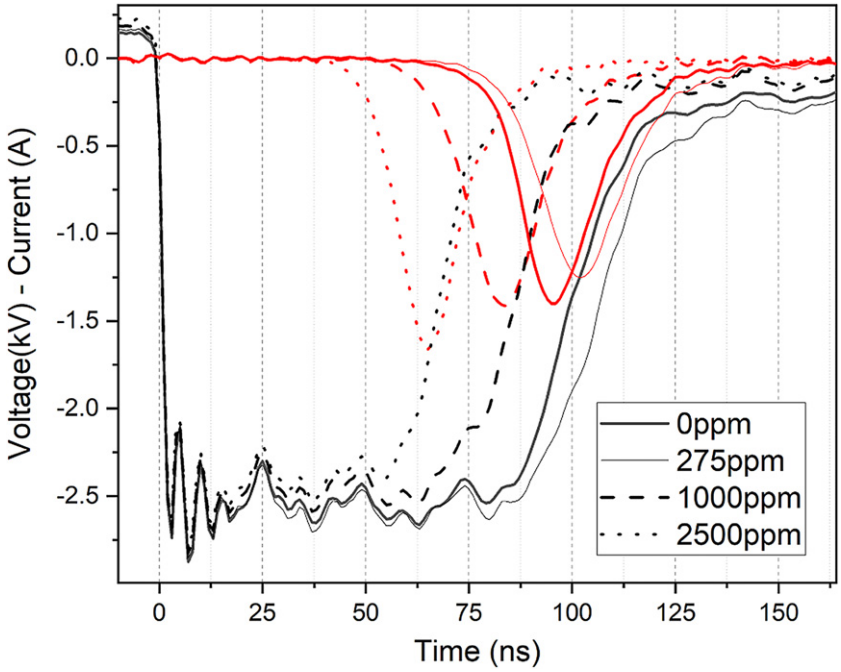

Figure 6. Voltage (black) and current (red) depending on H_2O initial concentration.

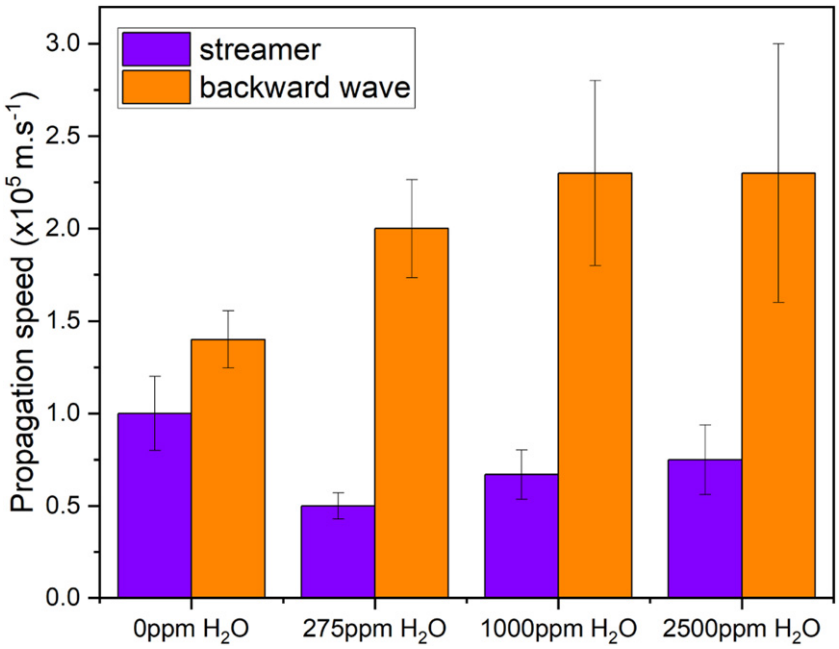

Figure 7. Chart of propagation speed and backward wave speed for the various gas mixtures.

He. According to simulations with the code GlobalKin, the remaining electron density just before the ignition of the next pulse is as high as 10^{18} m^{-3} in dry helium and would drop down to 10^{14} m^{-3}, whatever the water vapour concentration due to additional decay mechanisms involving water. Negative ion densities are found not to be significant. More background electrons at the start of the pulse explains the faster ignition and streamer propagation speed in dry helium compared to all humid conditions as observed experimentally.

On the other hand, the electron background density cannot explain the increasing streamer propagation speed with water vapour (275 to 2500 ppm). This effect probably comes instead from direct fast kinetics involving water molecules during propagation. In the channel of the streamer in dry helium, the ionisation is dominated by electron impact of helium atoms (predominantly by ionisation of ground state atoms during ignition and then quickly followed by ionisation of metastable atoms). In the presence of water vapour, Penning ionisation

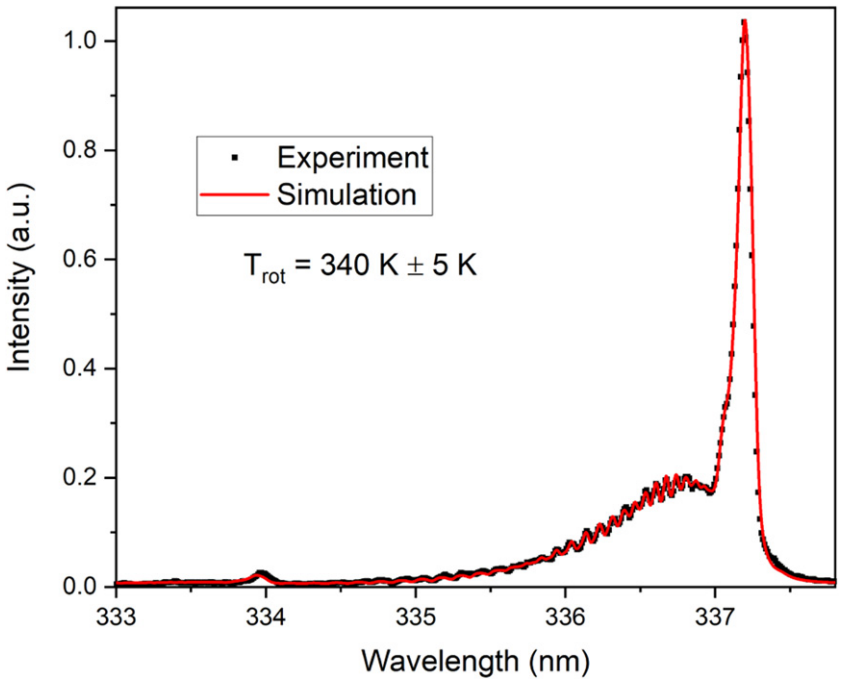

Figure 8. Experimental and simulated spectra of N_2(C−B)(0, 0) at 100 ns in 1000 ppm H_2O assuming rotational equilibrium.

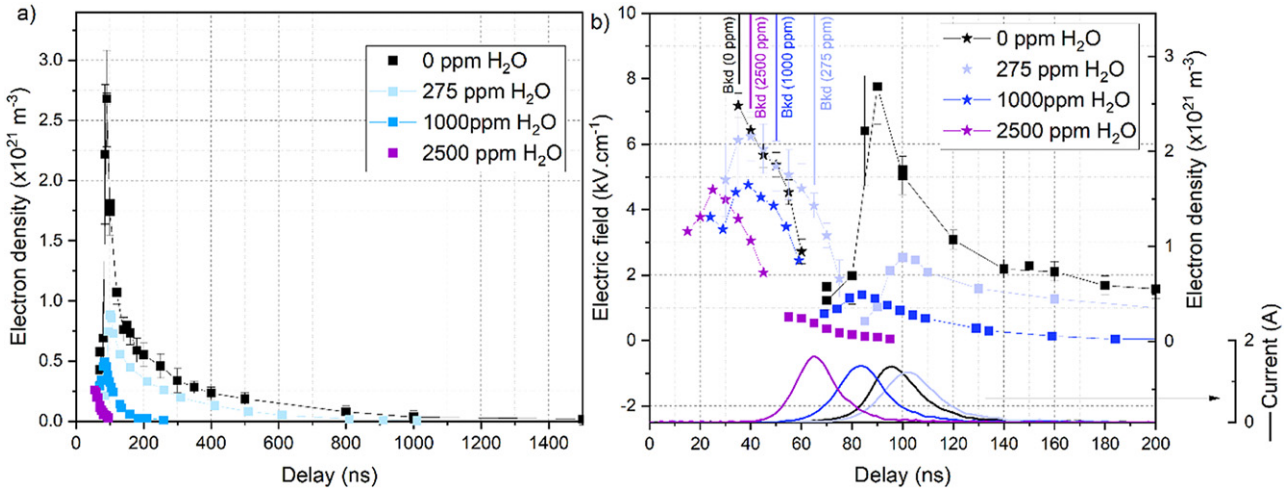

Figure 9. Electric field and electron densities in various gas mixtures measured at mid-gap by analysis of the Stark splitting and Stark broadening of the hydrogen beta line. The vertical lines labelled 'Bkd' on (b) refer to the instant of breakdown at the corresponding water vapour concentration.

((He +) He^M + H_2O → (He +) He + OH^+ + H + e) adds an effective, additional ionisation pathway that scales with increasing water content, independent of the electron density [8, 17]. The channel under humid conditions is therefore more conductive leading to lower electric fields, as presented in figure 9(b). With increasing conductivity of the channel, the remaining potential difference between the streamer head and the cathode increases helping to increase the speed of the streamer with increasing water content. Background electron density and increased ionisation rates in presence of water vapour could therefore explain the complex behaviour of propagation speed in this pin–pin glow discharge. To support these hypotheses, the code GlobalKin is run in dry helium and in He + 1000 ppm H_2O. Figure 10 represents the absolute production rates of electrons calculated by GlobalKin in both conditions. GlobalKin is a 0D model and does not resolve the spatial dimensions of the discharge and therefore does not capture the streamer and backward waves accurately in principle. However, the power implemented in GlobalKin is sharply peaked (from measurements) and the electric field simulated follows that trend: it is initially high and then stabilises to a lower value, close to that expected in the channel. This electric field behaviour is somewhat similar to that of the pulsed discharge for which the electric field and the electron density evolve in time at a given position. Therefore, as a first approximation, the results over time of the model could be interpreted

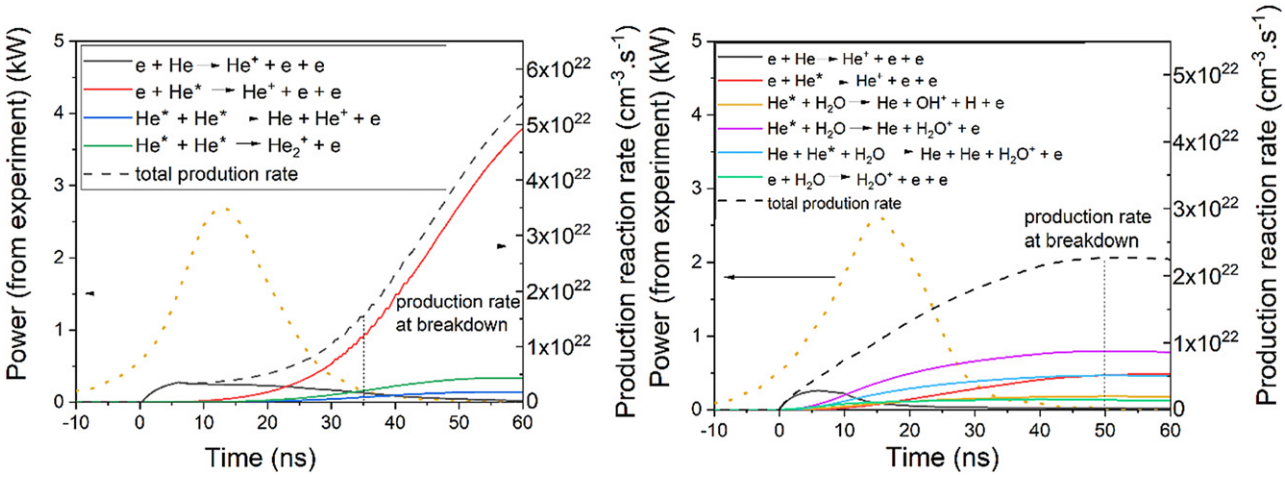

Figure 10. Absolute reaction rates for electron production according to GlobalKin in (a) dry helium (b) and He + 1000 ppm H_2O.

as the passage of the streamer head during the application of power, followed by the low electric field channel after the power drop. Results in figure 10 show the importance of direct ionisation of ground state helium in the streamer head for any conditions. Then, in dry helium, it is followed by ionisation of excited helium atoms after a few tens of nanoseconds (20 to 30 ns) and until breakdown. In He + 1000 ppm H_2O, Penning ionisation of water molecules starts and even dominates from the first tens of nanoseconds enhancing significantly the total electron production rate, suggesting faster propagation with increasing water concentration.

After breakdown, the channel conductivity and kinetics are quite different in dry and humid helium. The slower propagation with humidity leads to a strong growth of electron density before breakdown is established. This higher electron density at breakdown, in combination with the increased ionisation pathways, probably explains the faster backward wave in He + H_2O compared to dry He. Indeed, in dry helium, because the background electron density is significant before ignition, about 10^{18} m^{-3} as stated above, the streamer develops very fast and crosses the gap in only 30 ns. At such timescales, the growth of the electron density is rather limited and the channel remains relatively resistive at the instant of breakdown. Profiles of integrated light emission of the discharge (not shown here) reveal that excitation starts rising only at about 50 ns at mid gap, which confirms that the electron density did not have the time to grow significantly before breakdown. Therefore, in dry helium, fast streamer propagation leads to a slow backward wave. With humidity, despite the backward wave being fast, the situation is again complex. Indeed, it is possible that the faster streamer propagation with increasing humidity (leading to lower electron densities at breakdown) is compensated by the increasing ionisation rate with increasing water concentration, meaning that at the instant of breakdown, the channel density is similar for each water concentration studied leading eventually to a backward wave of similar speed for each water vapour concentration studied.

5.2. Electron decay

As shown in figure 9, in the afterglow, the decay of the electron density gets faster as the amount of water vapour in the gas mixture increases. This effect has already been described in a number of both RF and nanosecond pulsed helium discharges [8, 9, 41]. Nevertheless, even in dry helium, the electron decay in the gas phase is still a subject of discussion. It is generally agreed that the dominant process is electron–ion recombination with He_2^+. However, whereas several authors recommend the production of excited helium atoms in a two-body reaction [7, 42–44], other authors also consider three-body reactions which have very high recombination rates compared to the direct dissociation recombination, but for which the product is not yet very well known. This, and the fact that experimentally low radiative emission from molecular helium species is observed, lead Carbone *et al* [20], based on the works of Berlande *et al* [45], to suggest that a three-body reaction producing Rydberg states of the helium molecule is dominant. Other, in a very similar discharge to that of this work presented in [38], Verreycken *et al* suggests the electron decay in He + 500 ppm H_2O is due to a two-step process, first charge transfer from H^+, O^+, OH^+ and He^+ atoms to water and subsequent dissociative recombination of electrons with H_2O^+ and H_3O^+ forming OH. This assumption is based on the fact that the maximum electron density during the discharge corresponds to the maximum OH density in the afterglow measured by LIF but no kinetic model supports this hypothesis.

To help determine which processes govern the electron decay in the gas phase of the low-density mode pin–pin He + H_2O discharge, results from the Globalkin model are used. The aim is to identify the dominant processes and establish simplified kinetics models of the afterglow, which are compared to experiment. The species densities at the end of the discharge that are needed to run the kinetic models are inferred from results of the GlobalKin model (using the complete reaction set mentioned in section 3). To do so, the code is run for each concentration of water vapour added to the gas mixture and

Table 1. Chemical reactions considered to model the electron decay for four water vapour concentrations (M_1: dry He—M_2: He + 275 ppm H_2O—M_3: He + 1000 ppm H_2O—M_4: He + 2500 ppm H_2O). He∗ represents a lumped state of excited helium atoms including the metastable state He(2^3S).

Reaction	Reaction rate coefficient[a]	Model				References	Equation numbers
$e + He_2^+ \rightarrow He^* + He$	1.1×10^{-14}	M_1	M_2			[20, 30]	(3)
$He^+ + He + He \rightarrow He_2^+ + He$	1.21×10^{-43}	M_1	M_2	M_3	M_4	[46]	(4)
$He^* + He + He \rightarrow He_2^* + He$	2×10^{-46}		M_2			[47]	(5)
$e + H_2O \rightarrow OH + H^-$	$f(\varepsilon)$		M_2	M_3	M_4	[48, 49]	(6)
$He_2^* + H_2O \rightarrow He + He + H_2O^+ + e$	2.2×10^{-15}		M_2			[50]	(7)
$e + H_2O^+ \rightarrow O + H + H$	$f(T_e)$		M_2	M_3		[51, 52]	(8)
$e + O_2^+ \rightarrow O + O$	$f(T_e)$		M_2	M_3		[53]	(9)
$He^* + O_2 \rightarrow He + O_2^+ + e$	2.54×10^{-16}		M_2	M_3	M_4	[54]	(10)
$OH^+ + O_2 \rightarrow O_2^+ + OH$	5.9×10^{-16}		M_2	M_3		[51, 55]	(11)
$He_2^+ + O_2 \rightarrow He + He + O_2^+$	9×10^{-16}		M_2	M_3	M_4	[42, 56]	(12)
$He + O^+ + O \rightarrow He + O_2^+$	5×10^{-43}		M_2			[42]	(13)
$He_2^+ + O \rightarrow He + He + O^+$	2×10^{-15}		M_2			[42, 57–59]	(14)
$e + H_2O_3^+ \rightarrow O_2 + H_2O$	$f(T_e)$		M_2	M_3	M_4	[60]	(15)
$O_2^+ + H_2O \rightarrow H_2O_3^+$	Effective		M_2	M_3	M_4	[61]	(16)
$e + O_2 + He \rightarrow O_2^- + He$	$f(T_e)$			M_3	M_4	[62]	(17)
$H + O_2 \rightarrow HO_2$	Effective			M_3	M_4	[63, 64]	(18)
$H_3O^+ + H_2O \rightarrow H_5O_2^+$	Effective			M_3	M_4	[61, 65]	(19)
$e + H_5O_2^+ \rightarrow H + H_2O + H_2O$	$f(T_e)$			M_3	M_4	[40]	(20)
$OH^+ + H_2O \rightarrow H_3O^+ + O$	1.27×10^{-15}				M_4	[66]	(21)
$H_2O^+ + H_2O \rightarrow OH + H_3O^+$	2.05×10^{-15}				M_4	[66]	(22)
$e + H_4O_2^+ \rightarrow H + OH + H_2O$	$f(T_e)$				M_4	[60]	(23)

[a]In (m^3 s^{-1}) or (m^6 s^{-1}) for two and three body reactions.

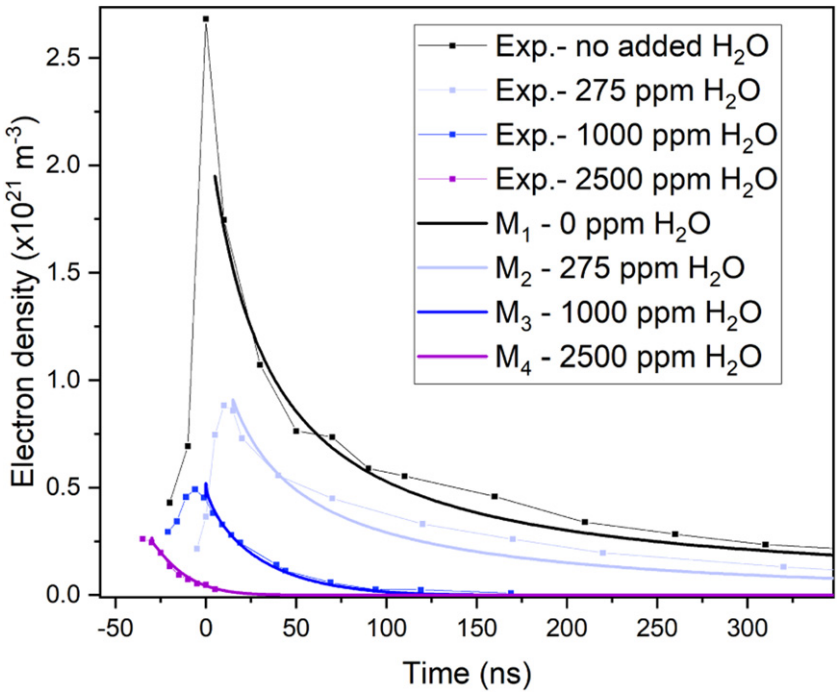

Figure 11. Electron density during the discharge and early afterglow and models of the electron decay depending on the concentration of water vapour.

the peak power input implemented in the code is adjusted so that the simulated and experimental peak electron densities are similar. Then, reactions of dominant production or consumption rates in the afterglow are identified. Despite GlobalKin being a 0D model, results in the afterglow should be reasonably accurate since there are very limited surface effects and the plasma is quite homogenous along the channel. The three-body reaction producing Rydberg states that was suggested in [20] and initially not included in GlobalKin, was not added in the final version due to its very fast reaction rate. Including it resulted in electron decay significantly faster than what was observed experimentally. Eventually, from the dominant

reactions identified for each condition, a simplified kinetic model is suggested. Each model is described in table 1 and the electron decay predicted by these simplified kinetics models (using the species densities predicted by the full model at the end of the discharge) is shown in figure 11 and appears to match the measured electron densities well.

From these models, it appears that in dry helium, the positive ion population is made up of He_2^+ and He^+. The measured electron decay rate (1.2×10^{-14} m^3 s^{-1}) corresponds to the recombination of electrons with the dominant ion He_2^+ (reaction (3)). Considering the conversion of He^+ into He_2^+ is essential to describe the complete recombination of electrons. Therefore reactions (3) and (4) of table 1 are sufficient to describe the electron decay even in presence of low impurity levels of water, here estimated to be of the order of 20 ppm H_2O experimentally.

With the addition of 275 ppm H_2O, water and the oxygen produced from water dissociation, start to play an important role in the electron decay. In particular, the reaction of dissociative attachment with water into OH and H^-, reaction (6), represents a significant contribution to the electron decay in the first nanoseconds of the afterglow, until the electron temperature has dropped significantly. Then recombination with He_2^+ and H_2O^+ (into 2H + O) become dominant and later in the afterglow dissociative recombination of O_2^+ and $H_2O_3^+$ should be considered. Note that the electron temperature remains elevated in the early afterglow, a few tenths of eV, due to superelastic collisions with excited helium atoms and excimers [41].

At increasing water vapour concentrations, the role of larger water induced species such as $H_2O_3^+$ and water clusters ($H^+(H_2O)_{n\leqslant 2}$) becomes important and dramatically accelerates the electron decay which only takes a few tens of nanoseconds at 2500 ppm H_2O. With increasing water concentration, large water clusters only have little influence on the electron decay because by the time they have built up from smaller clusters, the electrons have already significantly decayed.

6. Conclusions

A negative nanosecond pulsed discharge was generated in a pin–pin 3 mm gap geometry in He + H_2O. This geometry helps to achieve a good stability of the discharge, enables the study of volume kinetics due to minimal surface area, as well as provides a large optical access to the discharge. Measurements in this work allow the study of volume chemistry of He + H_2O for validation of kinetic models of plasmas in controlled environments.

The effect of humidity on the discharge development and on electron properties was also investigated. It was shown that in the presence of water vapour, the electric field is lower both in the streamer head and in the channel. Also, the electrons recombine more efficiently and the electron density remaining at the start of the next pulse is much lower than in dry helium. This results in a slower streamer propagation speed. On the other hand, due to a higher ionisation coefficient of water compared to helium, the discharge propagation speed increases with increasing water concentration. Also, at the point of breakdown, the conductivity in the channel is higher in humid conditions and eventually the current rise catches up with the dry case due to a faster backward wave.

The electron decay was studied using the 0D global kinetics model GlobalKin. The dominant reactions responsible for the electron decay depending on the concentration of water vapour were determined by comparing experimental and simulated results and these reactions were grouped in simplified kinetic models. It was found that even over a limited range of humidity (0–2500 ppm), the dominant decay mechanisms change significantly. In dry helium, the two-body dissociative recombination with He_2^+ seems to govern entirely the electron decay, while the three body recombination mechanism producing helium Rydberg state suggested in [20] seems too fast. At low water concentration, dissociative attachment to neutral water molecules followed by dissociative recombination of H_2O^+ and O_2^+ ions were highlighted. Even though the role of oxygen ions is strong, it seems that the two-step process suggested in [38] (charge transfer from hydrogen and oxygen ions to H_2O, followed by electron–water ion recombination leading to high OH densities), might not be dominant in this discharge. At large water concentrations, $H_2O_3^+$ and water clusters become the dominant species responsible for electron decay while He_2^+ ions are lost by dissociative charge transfer with O_2.

Acknowledgments

This work was supported by the EP/S026584/1 and EP/S025790/1 research programs. The authors would like to thank Professor Mark Kushner for providing the GlobalKin code used in this work, and for continued useful discussions.

Data availability statement

The data that support the findings of this study are available upon reasonable request from the authors.

ORCID iDs

Alexandra Brisset https://orcid.org/0000-0003-3217-1106
Benjamin Harris https://orcid.org/0000-0002-4036-8585
Aaron Dickenson https://orcid.org/0000-0003-4721-7138
Kari Niemi https://orcid.org/0000-0001-6134-1974
James Walsh https://orcid.org/0000-0002-6318-0892
Erik Wagenaars https://orcid.org/0000-0002-5493-3434

References

[1] Graves D B 2012 *J. Phys. D: Appl. Phys.* **45** 263001
[2] Reuter S, Tresp H, Wende K, Hammer M U, Winter J, Masur K, Schmidt-Bleker A and Weltmann K-D 2012 *IEEE Trans. Plasma Sci.* **40** 2986–93
[3] Lafleur T, Delattre P A, Johnson E V and Booth J P 2012 *Appl. Phys. Lett.* **101** 124104

[4] Invernizzi L, Muja C, Sainct F P and Guillot P 2020 *IEEE Trans. Radiat. Plasma Med. Sci.* **4** 121–9
[5] Shaw D, West A, Bredin J and Wagenaars E 2016 *Plasma Sources Sci. Technol.* **25** 065018
[6] Brisset A, Gibson A R, Schröter S, Niemi K, Booth J-P, O'Connell D and Wagenaars E 2021 *J. Phys. D: Appl. Phys.* **54** 285201
[7] Schröter S, Wijaikhum A, Gibson A R, West A, Davies H L, Minesi N, Dedrick J, Wagenaars E, de Oliveira N and Nahon L *et al* 2018 *Phys. Chem. Chem. Phys.* **20** 24263–86
[8] Liu D X, Bruggeman P, Iza F, Rong M Z and Kong M G 2010 *Plasma Sources Sci. Technol.* **19** 025018
[9] McKay K, Liu D X, Rong M Z, Iza F and Kong M G 2012 *J. Phys. D: Appl. Phys.* **45** 172001
[10] Ono R, Takezawa K and Oda T 2009 *J. Appl. Phys.* **106** 043302
[11] Dedrick J *et al* 2017 *J. Phys. D: Appl. Phys.* **50** 455204
[12] Simeni M S, Baratte E, Zhang C, Frederickson K and Adamovich I V 2018 *Plasma Sources Sci. Technol.* **27** 015011
[13] Pai D Z, Ostrikov K, Kumar S, Lacoste D A, Levchenko I and Laux C O 2013 *Sci. Rep.* **3** 1221
[14] Naidis G V, Tarasenko V F, Babaeva N Y and Lomaev M I 2018 *Plasma Sources Sci. Technol.* **27** 013001
[15] Brisset A, Gazeli K, Magne L, Pasquiers S, Jeanney P, Marode E and Tardiveau P 2019 *Plasma Sources Sci. Technol.* **28** 055016
[16] Leu M T, Biondi M A and Johnsen R 1973 *Phys. Rev.* A **7** 292–8
[17] Lazarou C, Chiper A S, Anastassiou C, Topala I, Mihaila I, Pohoata V and Georghiou G E 2019 *J. Phys. D: Appl. Phys.* **52** 195203
[18] Roettgen A, Shkurenkov I, Simeni Simeni M, Petrishchev V, Adamovich I V and Lempert W R 2016 *Plasma Sources Sci. Technol.* **25** 055009
[19] Schregel C-G, Carbone E A D, Luggenhölscher D and Czarnetzki U 2016 *Plasma Sources Sci. Technol.* **25** 054003
[20] Carbone E A D, Schregel C-G and Czarnetzki U 2016 *Plasma Sources Sci. Technol.* **25** 054004
[21] Popov M A, Kochetov I V, Starikovskiy A Y and Aleksandrov N L 2018 *J. Phys. D: Appl. Phys.* **51** 264003
[22] Podolsky V and Macheret S 2019 *Plasma Sources Sci. Technol.* **28** 055008
[23] Bruggeman P, Schram D, González M Á, Rego R, Kong M G and Leys C 2009 *Plasma Sources Sci. Technol.* **18** 025017
[24] Verreycken T, van der Horst R M, Baede A H F M, Van Veldhuizen E M and Bruggeman P J 2012 *J. Phys. D: Appl. Phys.* **45** 045205
[25] Laux C O, Spence T G, Kruger C H and Zare R N 2003 *Plasma Sources Sci. Technol.* **12** 125–38
[26] van der Horst R M, Verreycken T, van Veldhuizen E M and Bruggeman P J 2012 *J. Phys. D: Appl. Phys.* **45** 345201
[27] Gigosos M A, González M Á and Cardeñoso V 2003 *Spectrochim. Acta* B **58** 1489–504
[28] Bastien F and Marode E 1977 *J. Quant. Spectrosc. Radiat. Transfer* **17** 453–69
[29] Videnović I R, Konjević N and Kuraica M M 1996 *Spectrochim. Acta* B **51** 1707–31
[30] Johnson A W and Gerardo J B 1972 *Phys. Rev.* A **5** 1410–8
[31] Du Y, Nayak G, Oinuma G, Peng Z and Bruggeman P J 2017 *J. Phys. D: Appl. Phys.* **50** 145201
[32] Vasko C A, Liu D X, van Veldhuizen E M, Iza F and Bruggeman P J 2014 *Plasma Chem. Plasma Process.* **34** 1081–99
[33] Wang Q, Doll F, Donnelly V M, Economou D J, Sadeghi N and Franz G F 2007 *J. Phys. D: Appl. Phys.* **40** 4202–11
[34] Bruggeman P J, Sadeghi N, Schram D C and Linss V 2014 *Plasma Sources Sci. Technol.* **23** 023001
[35] Voráč J, Synek P, Procházka V and Hoder T 2017 *J. Phys. D: Appl. Phys.* **50** 294002
[36] Voráč J, Synek P, Potočňáková L, Hnilica J and Kudrle V 2017 *Plasma Sources Sci. Technol.* **26** 025010
[37] Voráč J, Kusýn L and Synek P 2019 *Rev. Sci. Instrum.* **90** 123102
[38] Verreycken T, Sadeghi N and Bruggeman P J 2014 *Plasma Sources Sci. Technol.* **23** 045005
[39] Naidis G V 2011 *Appl. Phys. Lett.* **98** 141501
[40] Huang B-D, Carbone E, Takashima K, Zhu X-M, Czarnetzki U and Pu Y-K 2018 *J. Phys. D: Appl. Phys.* **51** 225202
[41] Simeni M S, Roettgen A, Petrishchev V, Frederickson K and Adamovich I V 2016 *Plasma Sources Sci. Technol.* **25** 064005
[42] Turner M M 2015 *Plasma Sources Sci. Technol.* **24** 035027
[43] Turner M M 2016 *Plasma Sources Sci. Technol.* **25** 015003
[44] Golubovskii Y B, Maiorov V A, Behnke J and Behnke J F 2002 *J. Phys. D: Appl. Phys.* **36** 39–49
[45] Berlande J, Cheret M, Deloche R, Gonfalone A and Manus C 1970 *Phys. Rev.* A **1** 887–96
[46] Bohringer H, Glebe W and Arnold F 1983 *J. Phys. B: At. Mol. Phys.* **16** 2619–26
[47] Myers G and Cunningham A J 1977 *J. Chem. Phys.* **67** 247–53
[48] Itikawa Y and Mason N 2005 *J. Phys. Chem. Ref. Data* **34** 1–22
[49] Melton C E and Neece G A 1971 *J. Am. Chem. Soc.* **93** 6757–9
[50] Pouvesle J M, Stevefelt J, Lee F W, Jahani H R, Gylys V T and Collins C B 1985 *J. Chem. Phys.* **83** 2836–9
[51] McElroy D, Walsh C, Markwick A J, Cordiner M A, Smith K and Millar T J 2013 *Astron. Astrophys.* **550** A36
[52] Rosén S *et al* 2000 *Faraday Discuss.* **115** 295–302
[53] Peverall R *et al* 2001 *J. Chem. Phys.* **114** 6679–89
[54] Pouvesle J M, Khacef A, Stevefelt J, Jahani H, Gylys V T and Collins C B 1988 *J. Chem. Phys.* **88** 3061–71
[55] Jones J D C, Birkinshaw K and Twiddy N D 1981 *Chem. Phys. Lett.* **77** 484–8
[56] Ikezoe Y 1987 *Gas Phase Ion–Molecule Reaction Rate Constants through 1986* (Ion Reaction Research Group of the Mass Spectroscopy Society of Japan) https://doi.org/10.1002/rcm.1290030312
[57] Eichelberger B R, Snow T P and Bierbaum V M 2003 *J. Am. Soc. Mass Spectrom.* **14** 501–5
[58] Langevin M P 1905 *Ann. Chim. Phys.* **5** 245–88
[59] Miller T M 2000 Atomic and molecular polarizabilities *CRC Handbook of Chemistry and Physics* vol 77 (Boca Raton, FL: CRC Press) pp 193–202
[60] Bortner M H and Baurer T 1978 *Defense Nuclear Agency Reaction Rate Handbook* 2nd edn (Philadelphia, PA: General Electric Co., Space Div.) revision number 7
[61] Sieck L W, Heron J T and Green D S 2000 *Plasma* **20** 235–58
[62] Itikawa Y, Ichimura A, Onda K, Sakimoto K, Takayanagi K, Hatano Y, Hayashi M, Nishimura H and Tsurubuchi S 1989 *J. Phys. Chem. Ref. Data* **18** 23–42
[63] Atkinson R, Baulch D L, Cox R A, Crowley J N, Hampson R F, Hynes R G and Jenkin M E 2004 *Atmos. Chem. Phys.* **4** 1461–738
[64] Hsu K J, Durant J L and Kaufman F 1987 *J. Phys. Chem.* **91** 1895–9
[65] Lau Y K, Ikuta S and Kebarle P 1982 *J. Am. Chem. Soc.* **104** 1462–9
[66] Huntress W T and Pinizzotto R F 1973 *J. Chem. Phys.* **59** 4742–56